STP 1637, 2022 / available online at www.astm.org / doi: 10.1520/STP163720200125

Andreas Fischer,[1] Malte Vollmer,[1] Philipp Krooß,[1] and Thomas Niendorf[1]

Microstructural and Mechanical Properties of AISI 4140 Steel Processed by Electron Beam Powder Bed Fusion Analyzed Using Miniature Samples

Citation

A. Fischer, M. Vollmer, P. Krooß, and T. Niendorf, "Microstructural and Mechanical Properties of AISI 4140 Steel Processed by Electron Beam Powder Bed Fusion Analyzed Using Miniature Samples," in *Progress in Additive Manufacturing 2020*, ed. N. Shamsaei and M. Seifi (West Conshohocken, PA: ASTM International, 2022), 296–311. http://doi.org/10.1520/STP163720200125[2]

ABSTRACT

The present study reports on the identification of an adequate process window for electron beam powder bed fusion (E-PBF) of AISI 4140 steel. For characterization, only miniature samples were used. It is clearly revealed that, for comparison and evaluation of different conditions, the use of such small samples is absolutely sufficient, even under fatigue loading. The initial E-PBF as-built condition is compared with conventionally heat-treated conditions (i.e., normalized as well as quenched and tempered). Based on the results obtained, the advantages of E-PBF in comparison to other additive manufacturing routes, such as laser powder bed fusion (L-PBF), are discussed. In E-PBF, a very ductile material behavior results from the prevailing process conditions. Furthermore, an as-built condition almost free of residual stresses is established by E-PBF. Microstructural as well as fracture surface analyses were conducted and further supported by three-dimensional defect characterization applying X-ray computed tomography. It was found that

Manuscript received December 22, 2020; accepted for publication February 18, 2021.

[1]University of Kassel, Institute of Materials Engineering—Metallic Materials, Moenchebergstr. 3, 34125, Kassel, Germany M. V. https://orcid.org/0000-0002-8098-8498, P. K. https://orcid.org/0000-0001-8310-9631, T. N. https://orcid.org/0000-0003-2622-5817

[2]ASTM *International Conference on Additive Manufacturing* held virtually on November 16–20, 2020.

the microstructural appearance of the as-built condition is affected most severely by the relatively sluggish cooling after the uppermost layer is finished. Thus, many issues related to L-PBF processing of carbon steels such as AISI 4140 do not prevail in E-PBF. The results obtained by mechanical testing clearly reveal that the remaining process-related volume defects can be compensated to a certain extent in the ductile as-built state. Consequently, the non-heat-treated, as-built condition is characterized by fatigue properties similar to those of post-treated AISI 4140. The latter, however, is characterized by superior strength under monotonic loading.

Keywords
electron beam melting, additive manufacturing, microstructure, heat treatment, mechanical performance, structural integrity

Introduction

In recent years, powder bed-based additive manufacturing (AM) processes such as electron beam powder bed fusion (E-PBF), also referred to as PBF-EB/M or electron beam melting (EBM), have attracted significant attention.[1,2] In numerous industrial fields, E-PBF is already widely established.[3,4] Zadi-Maad, Rohib, and Irawan[5] published an overview focusing on technically relevant alloys (e.g., AISI 316L) that can already be robustly produced using different AM processes. However, up to now, the E-PBF community focused mainly on titanium alloys.[6–8]

In comparison to competing additive manufacturing processes, such as laser powder bed fusion (L-PBF or PBF-LB/M), also referred to as selective laser melting (SLM),[9] E-PBF has numerous advantages due to the high deflection speed of the electron beam, the characteristic vacuum conditions, as well as the high powder bed temperatures realized by preheating of each material layer.[10] In particular, preheating of each powder layer leads to a relatively slow cooling rate of the manufactured samples, eventually allowing reliable processing of high-carbon steels as well as brittle and highly reactive materials.[11] Moreover, high thermal gradients resulting from large temperature differences between the processed part and the powder layer can be avoided and, thus, detrimental residual stresses can be minimized. Thus, powder preheating seems to be particularly important for quenched and tempered steels. In this regard, E-PBF can be compared with a microwelding process, where a carbon-dependent preheating temperature level often is required.[12]

From an industrial point of view, interest in AM of quenched and tempered steels, such as the AISI 4140, is steadily increasing due to the wide range of potential applications as well as its inherent cost efficiency and tailorable mechanical properties set by adequate post treatments.[13,14] E-PBF seems to be well suited for robust processing of such alloys. However, due to the unavoidable presence of at least a minor number of process-induced defects, such as porosity, lack of fusion, or cracking, data reporting on the resulting fatigue properties is crucially needed to assess the manufacturability of safe and reliable structures via E-PBF.[15,16] In particular, a deep understanding of the

elementary mechanisms being promoted by cyclic loading is crucial as mechanisms can differ considerably from quasistatic loading conditions.[17]

The research questions addressed by the present work include two main aspects: Are the microstructural and mechanical properties of AISI 4140 following E-PBF processing sufficient for the envisaged robust industrial applications? Can a thorough evaluation of such properties be conducted based only on miniature samples?

Material and Methods

AISI 4140 samples were processed using nitrogen atomized powder with a particle size distribution ranging from 54 µm to 108 µm and a nominal chemical composition of (in wt.%): 0.41% carbon (C), 0.36% silicon (Si), 0.79% manganese (Mn), 1.1% chromium (Cr), 0.22% molybdenum (Mo), and the balance iron (Fe). Cuboid blocks with dimensions of 10 mm by 10 mm by 50 mm were built using an E-PBF system (Arcam EBM Model A2X). A substrate plate with dimensions of 150 mm by 150 mm by 10 mm was used and heated to 920°C with a dwell time of 30 min. For the entire manufacturing process, a layer thickness of 50 µm was applied. ARCAM auto functions were enabled. The surface contour of the cuboid blocks was processed at a volume energy density, in the following referred to as volume energy, of 45 J/mm^3. A schematic temperature-time profile representative of the process as well as the scanning strategy employed will be shown later in the results and discussion.

The as-built condition was subjected to different well-established heat treatments, that is, normalization as well as two quenching and tempering routes (QT1 and QT2). In the case of normalization, the samples were heat treated at 850°C for 20 min followed by air cooling to room temperature. The quenched and tempered conditions were austenitized for 20 min at a temperature level of 850°C and afterward quenched in oil. Based on an expected martensite finish temperature of 120°C, the temperature of the oil bath was set to 90°C. Oil quenching was followed by air cooling in order to ensure a complete martensitic transformation, and to avoid pronounced sample distortion and hardening cracks.[18] Subsequently, the hardened samples were tempered for 60 min at 350°C (QT1) and 600°C (QT2), respectively.

In addition to optical microscopy and hardness measurements (HV) for characterization of the different conditions, microstructural and fracture analyses were conducted using a Zeiss Ultra Plus scanning electron microscope (SEM) operated at an acceleration voltage of 20 kV. The SEM used was equipped with an electron backscatter diffraction (EBSD) unit. Furthermore, a Zeiss Xradia 520 Versa µ-computed tomography (µ-CT) system was employed. Measurements were carried out using an acceleration voltage of 80 kV and a power of 7 W. The evaluation of the µ-CT data was carried out using Avizo 9.4.0 software (Thermo Scientific).

Due to the miniature sample geometries employed in present work, tests did not exactly follow an approved test standard. All relevant details for these tests are given as follows: Uniaxial tensile tests were conducted at room temperature using a screw-driven MTS Criterion load frame equipped with a 20 kN load cell. The tests were performed under displacement control with a constant crosshead speed of 2 mm/min. Furthermore, an MTS miniature extensometer with a gauge length of 5 mm was directly attached to the surface of the samples. In each material condition, three samples were tested.

Cyclic tests were conducted at predefined stress amplitudes at ambient temperature. A Schenck servohydraulic testing machine equipped with a 63 kN load cell was used to perform the fatigue experiments at 25 Hz. Fatigue tests were carried out under fully reversed push-pull loading at a constant total stress amplitude ($R = -1$). For each material condition and loading amplitude, three samples were tested. Median calculations were made on the basis of the three values determined in each case. All samples were cut using electro discharge machining from the E-PBF processed blocks. Differences regarding the sample geometries used for the monotonic (i.e., quasistatic) and cyclic mechanical tests are detailed in figure 1*A* and *B*. All samples were mechanically ground stepwise and then polished using a colloidal silica solution of 0.04 µm for 2 h in order to eliminate surface roughness.

Angle-dispersive X-ray diffraction (XRD) measurements were performed using a D5000 diffractometer equipped with a Cr tube source. The classical $\sin^2\text{-}\Psi$ method including layer removal was employed for determination of in-depth residual stress profiles.[19] A similar XRD system was used for phase analysis.

FIG. 1 Miniature sample geometry used for mechanical testing: (*A*) tensile tests and (*B*) fatigue tests. All dimensions are in mm.

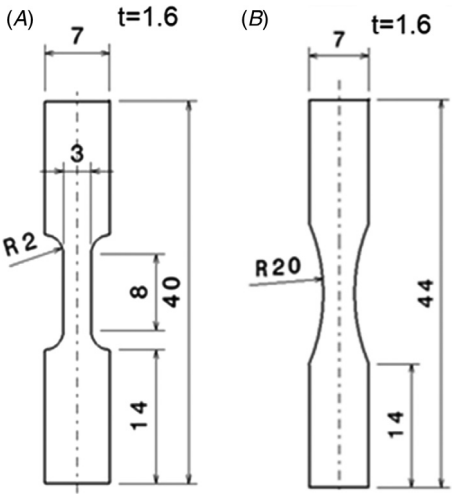

Results and Discussion

The general characteristics of the nitrogen atomized AISI 4140 initial powder were analyzed by means of µ-CT and SEM. Results are shown in figure 2*A* and *B*. An average particle size of 64.3 µm was determined. Furthermore, a sphericity of 0.92 was calculated based on the three-dimensional data shown in figure 2*A*. The sphericity of 0.92 is in line with the irregular shape of the powder particles illustrated by the SEM results in figure 2*B* (i.e., numerous powder particles shown are not perfectly spherical in shape). The relatively high fraction of irregularly shaped powder particles, some of them additionally being characterized by satellite features on the surface, can be seen in figure 2*B*.

Following initial characterization of the powder, parameter studies were conducted to establish an adequate parameter set for E-PBF processing of AISI 4140. Details are provided in tables 1 and 2, where the parameters used to manufacture cuboid blocks are listed. In the first step, volume energies ranging from 40.8 to 68 J/mm^3 were considered based on the authors' experience stemming from E-PBF processing of other steels. Different volume energies were set by varying the beam

FIG. 2 Initial AISI 4140 powder characterized by (*A*) µ-CT analysis and (*B*) SEM analysis.

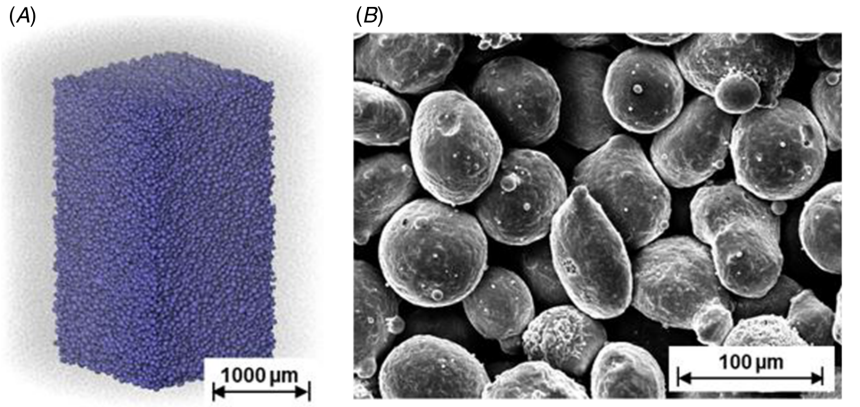

TABLE 1 First-level parameter study

		Beam Current / (mA)		
		7.5	8.0	8.5
Scanning Speed *v* (mm/s)	1,500	60	64	68
	2,000	45	48	51
	2,500	36	38.4	40.8

Note: Varying beam currents and scanning speeds result in different volume energies (J/mm^3).

TABLE 2 Second-level parameter study

		Beam Current *I* (mA)				
		1.875	3.75	7.5	15	30
Hatch *h* (mm)	0.025	45				
	0.05		45			
	0.1			45		
	0.2				45	
	0.4					45

Note: The volume energy was kept constant at 45 J/mm^3 by adequately varying the beam current and hatch simultaneously. Scanning speed was kept constant at 2,000 mm/s. Medium and dark gray process combinations are examined in detail in the remainder of this work.

current and the scanning speed according to table 1, whereas the layer thickness of 50 µm as well as a hatch of 0.1 mm were kept constant. Within the chosen parameter field, the most promising results with respect to the highest material density were obtained for a beam current of 7.5 mA and a scanning speed of 2,000 mm/s, resulting in a volume energy of 45 J/mm^3 (marked in dark gray in table 1). A representative micrograph for this parameter set is shown in figure 3*A*. It is important to note that small pores still prevail.

In the second-level parameter study (table 2), additional parameter variations were considered on the basis of an equal volume energy of 45 J/mm^3 (starting point marked in dark gray. As the microstructure can be significantly influenced by varying the hatch,[20,21] this process parameter was varied along with the beam current. The resulting process parameter combinations can be seen in table 2. Although the same volume energy of 45 J/mm^3 was applied in each case, significant microstructural differences resulted from these parameter combinations. Figure 3*B* through *D* highlight corresponding microstructural features revealed by microstructural analysis.

A small hatch of 0.025 mm, in combination with a low beam current of 1.875 mA, results in a microstructure being characterized by cracks alongside the grain boundaries in build direction (BD), as shown in figure 3*B*. On the contrary, a large hatch of 0.4 mm in combination with a high beam current of 30 mA (marked in light gray) led to a microstructure being characterized by a high defect density, where defects were significantly different in appearance. The corresponding micrograph can be seen in figure 3*C*. The apparent volume defects have evolved transversely to the build direction. The highest material density was obtained by applying a beam current of 3.75 mA and a hatch of 0.05 mm (labeled in medium gray). As displayed in figure 3*D*, a lower porosity (as compared to figure 3*A*) can be clearly seen. Based on these results, cuboid blocks for further investigations were manufactured using only the melting parameters detailed in figure 3*D*.

A representative volume element obtained by the three-dimensional defect analysis conducted by µ-CT for the E-PBF as-built state of the cuboid blocks can be seen in figure 4. A relative density of 99.94% was determined from this volume.

FIG. 3 Optical micrographs of samples manufactured using a constant layer thickness of 50 µm and a scanning speed of 2000 mm/s and different hatch distances and beam currents: (A) h = 0.1 mm and I = 7.5 mA (B) h = 0.025 mm and I = 1.875 mA, (C) h = 0.4 mm and I = 30 mA, (D) h = 0.05 mm and I = 3.75 mA (compare, tables 1 and 2).

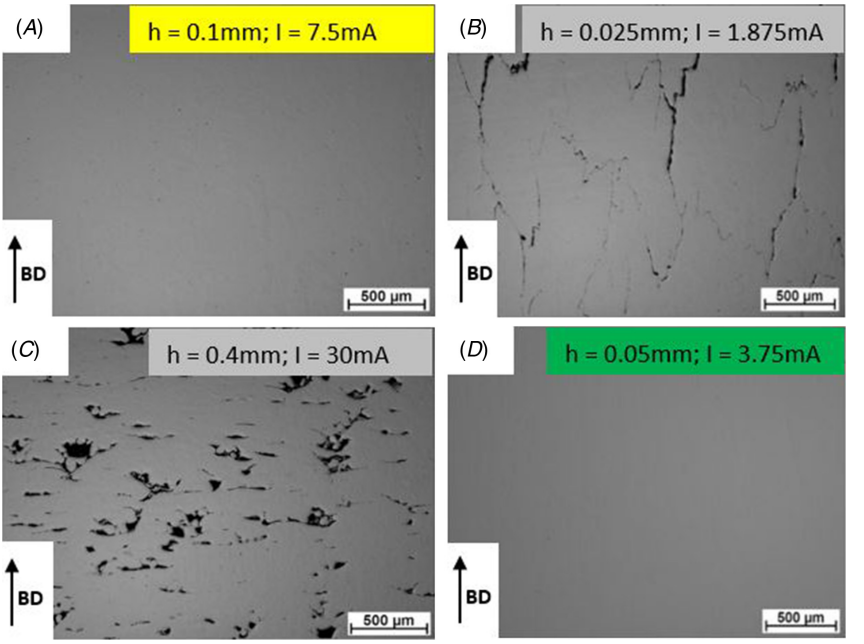

FIG. 4 µ-CT defect analysis for E-PBF AISI 4140 steel samples in the as-built condition processed based on the optimized parameter set (medium grey) listed in table 2.

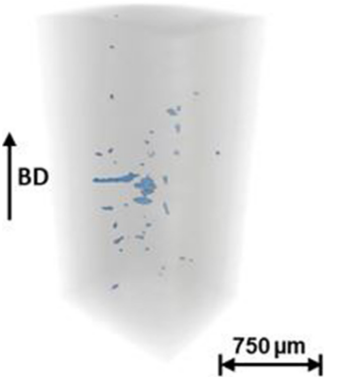

The recognizable volume defects are characterized by disc-shaped cavities of varying sizes. These volume defects were predominantly found in the transverse direction with respect to the BD.

In addition, XRD measurements were performed. It can be seen from the diffractograms shown in **figure 5*A*** that the line positions of the α-phase (ferrite) can be clearly assigned. In addition, the intensity peaks highlighted by the circles can be linked to carbide phases being present in AISI 4140.[22] The in-depth profiles of residual stresses obtained by XRD, with absolute values well below 100 MPa, are detailed in **figure 5*B*** for the as-built condition. The integral width values of the as-built state reveal homogeneous distributions (between 1.97° and 2.01°) independent of the measuring direction.

FIG. 5 X-ray diffraction analysis: (*A*) intensity profile for phase analysis in the as-built state and (*B*) in-depth residual stress as well as integral width profiles.

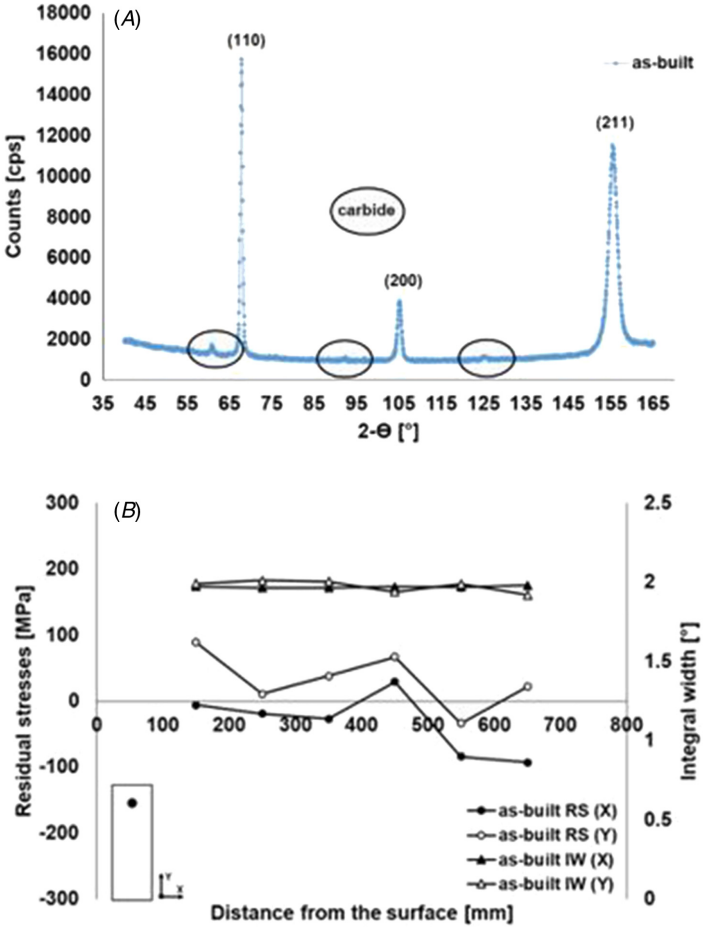

As already mentioned, three different heat treatment procedures, that is, a normalization heat treatment as well as quenching and tempering (QT1 and QT2), were considered in the present work. For comprehensive microstructural characterization, optical microscopy and EBSD measurements were carried out (**fig. 6**). EBSD results shown in **figure 6** (image quality superimposed with inverse pole figure maps) are plotted with respect to BD. A preferred crystallographic orientation of the microstructure could not be identified in any case. On the basis of the optical micrograph of the as-built state shown in **figure 6*A***, elongated structures aligned alongside the BD can be seen. It is important to note that this microstructure is clearly different from many other steels processed by AM and E-PBF (e.g., AISI 316L) as can be directly deduced from the EBSD results (**fig. 6*B***). At first glance, microstructural evolution seems to be in good agreement with the continuous time-temperature-transformation (TTT) diagram of AISI 4140.[23] An average hardness level of 243.2 HV0.5 seems to be in a reasonable range as compared to values reported for this alloy in the literature (assuming the presence of ferrite, pearlite, and bainite upon relatively slow cooling). Obviously, in the higher-magnified EBSD orientation map, shown in **figure 6*B***, the columnar structures can hardly be seen anymore. Here, finely distributed subgrain structures are visible. However, it is important to note that the microstructure is different from E-PBF processed austenitic steels such as AISI 316L. Solidification of the AISI 4140 is rather ferritic, such that multiple phase transformations induced by intrinsic heat treatment significantly affect final microstructure appearance. Furthermore, the microstructure

FIG. 6 Optical and EBSD micrographs (superimposed image quality and inverse pole figure maps) of E-PBF AISI 4140 steel in different material states: (*A*) and (*B*) as built, (*C*) and (*D*) normalized, (*E*) and (*F*) QT1, and (*G*) and (*H*) QT2. Please note the differences in the scale bars.

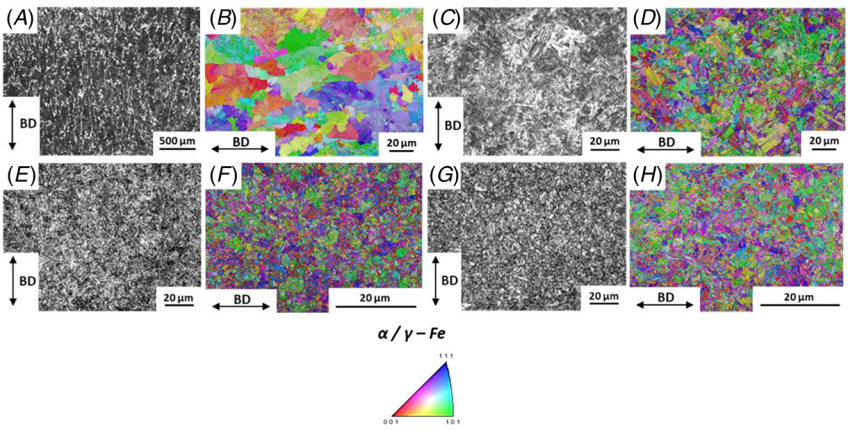

shown in figure 6*A* and *B* is primarily affected by sluggish cooling after the final layer in the E-PBF process is molten.

As is highlighted in the schematic shown in figure 7*A*, final cooling indeed is slow due to the process environment. Depending on the final build layout, cooling can be in the range of hours. Thus, as is indicated by XRD phase analysis as well as optical and EBSD micrographs, the microstructure of the as-built condition is primarily ferritic-pearlitic. Significant amounts of bainite are not resolved by the techniques employed. Obviously, hardness is higher than expected for such a type of microstructure. TTT diagrams predict significantly lower hardness at this point.[23] In terms of the prevailing microstructure shown in figure 6*A*, however, the unique appearance of the AISI 4140 processed by E-PBF has to be taken into account. Obviously, the cell-like arrangements surrounding the slightly elongated features

FIG. 7 Hardness mappings of E-PBF AISI 4140 for different material states: (*A*) as built with a schematic temperature-time profile of the E-PBF process shown to the right, (*B*) normalized, (*C*) QT1, and (*D*) QT2.

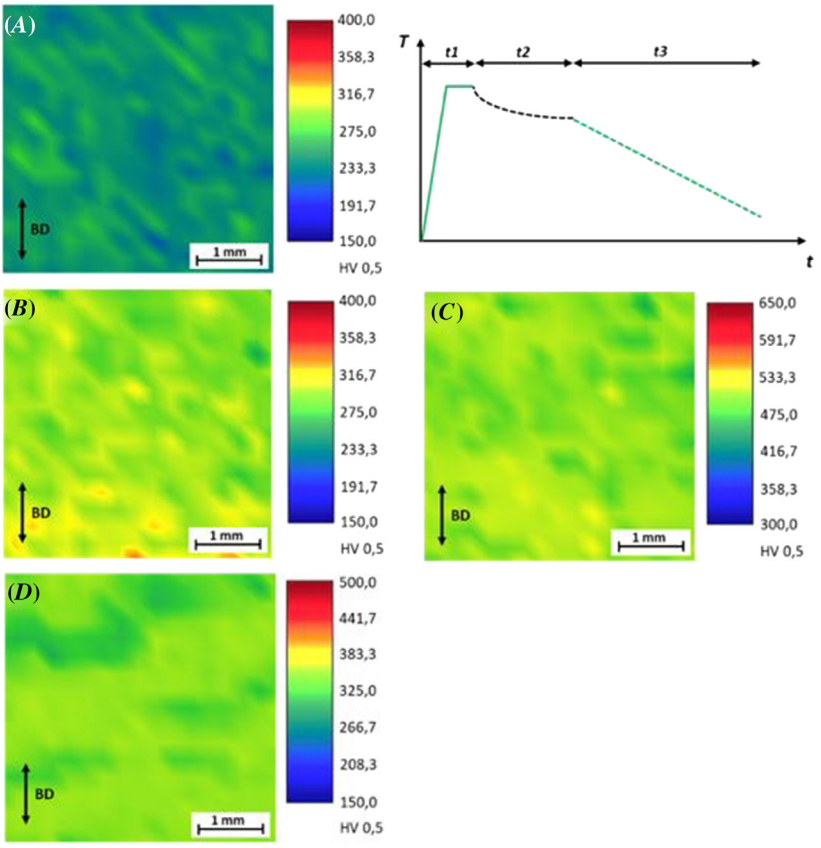

seen in the optical micrograph have to be considered. The dominant influence of cell structures in numerous AM alloys has already been discussed in the literature; however, its role in terms of AISI 4140 remains unclear so far. Future work will have to shed light on this aspect.

After normalization (**fig. 6*C***), a more homogeneous microstructure with respect to the overall grain morphology can be seen. The previously visible columnar grain structure alongside BD can no longer be observed. Taking into account a hardness level of 298 HV0.5 and the already mentioned continuous TTT diagram,[23] the microstructure shown can be characterized as a ferritic-bainitic structure, as is known for air-cooled conditions of AISI 4140. At the same time, normalization seems to lead to a significantly reduced average grain size, which is obvious from direct comparison of **figure 6*B*** and ***D***. Moreover, the initial subgrain structure can no longer be observed. After quenching and tempering, that is, in conditions referred to as QT1 (**fig. 6*E*** and ***F***) and QT2 (**fig. 6*G*** and ***H***), very fine-grained homogeneous microstructures showing needle-like features prevail in both cases. Based on evaluation of the experimentally determined hardness levels of 502.5 HV0.5 (QT1) and 345.3 HV0.5 (QT2), a microstructure consisting of tempered martensite prevails in both cases. As is well known from conventionally processed AISI 4140, tempering temperature has a major impact on final hardness (i.e., a higher tempering temperature leads to lower hardness values).

The average hardness values mentioned in the previous section were deduced from the hardness mappings shown in **figure 7*A*** through ***D***, with each map based on 289 indents. In line with the previously shown optical micrographs, no detrimental inhomogeneities imposed by E-PBF or the corresponding heat treatments can be seen. In particular, it should be noted that the E-PBF as-built condition in **figure 7*A*** already is characterized by a homogeneous hardness level across the complete volume probed. The graph on the right-hand side shows the characteristic temperature-time profile during the entire E-PBF process schematically, including preheating (t_1), the build process (t_2), and sample cooling upon final melting to room temperature (t_3).

Figure 8 shows stress-strain curves obtained by tensile tests of the four investigated material conditions (i.e., as built, normalized, QT1, and QT2). The stress-strain diagrams of the tensile tests reveal significant differences in terms of material performance (i.e., different yield and tensile strengths as well as elongation at fracture). In the as-built state, a maximum ultimate tensile stress of around 850 MPa and an elongation at fracture ranging from 12% to 14% can be observed, eventually revealing a fairly ductile material condition. All other conditions clearly show superior strength but inferior ductility.

In the case of all fracture surfaces shown in **figure 8*B*** through ***E***, well-known fracture patterns, which are characterized by pronounced roughness, can be seen. However, distinct, island-like features are revealed perpendicular to the tensile direction in all conditions. As highlighted by the black arrows in **figure 8*B***, these areas are characterized by very smooth surfaces. Furthermore, it should be noted

FIG. 8 Stress-strain curves obtained by tensile tests for E-PBF AISI 4140 in different material conditions: (*A*) as built, normalized, QT1, and QT2 conditions. Corresponding fracture surfaces are shown for: (*B*) as built, (*C*) normalized, (*D*) QT1, and (*E*) QT2. The insets in (*A*) highlight the scanning strategy considered in the present work, where each subsequent layer has been rotated by 90°.

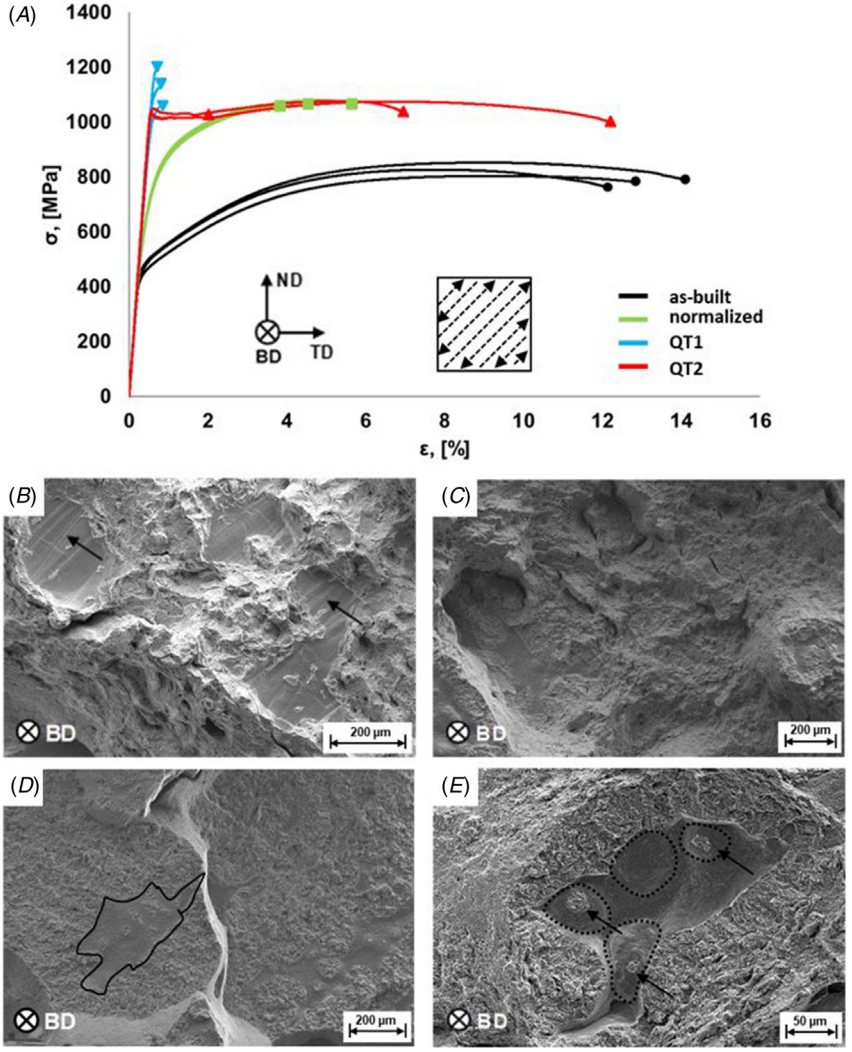

that the smooth areas are present in direct vicinity to dimple-like structures, which are known to be characteristic for ductile fractures.[24]

As detailed in figure 9*A*, the fatigue strength in the as-built condition was determined using the classical staircase method according to the evaluation method of

Hück, referred to as the *IABG method*.[16] Due to the large number of microstructural defects (cf. **fig. 6**), the starting amplitude of 150 MPa was defined at a very low level (**fig. 9A**). An estimation of the starting amplitude based on the tensile strength was refrained from due to pronounced scattering.[25,26] The test series for estimating fatigue strength was accomplished based on six samples, thus meeting the minimum required number of samples.[16] With respect to the corresponding equation according to the IABG method, an average fatigue strength of about 191 MPa is established for the as-built condition. Based on this result, three different loading amplitudes (210 MPa, 270 MPa, and 330 MPa) within the high-cycle fatigue regime were defined for the cyclic tests. In addition to the results obtained from tests in the BD (longitudinal), the QT2 condition was also tested in the transverse direction

FIG. 9 Fatigue tests: (*A*) Determination of fatigue strength of the as-built condition according to the staircase method, (B) S-N curves (high-cycle fatigue, stress amplitudes in MPa) for the as-built condition (longitudinal) and the quenched and tempered QT2 state (longitudinal and transverse). Experimentally determined values are labeled as x.

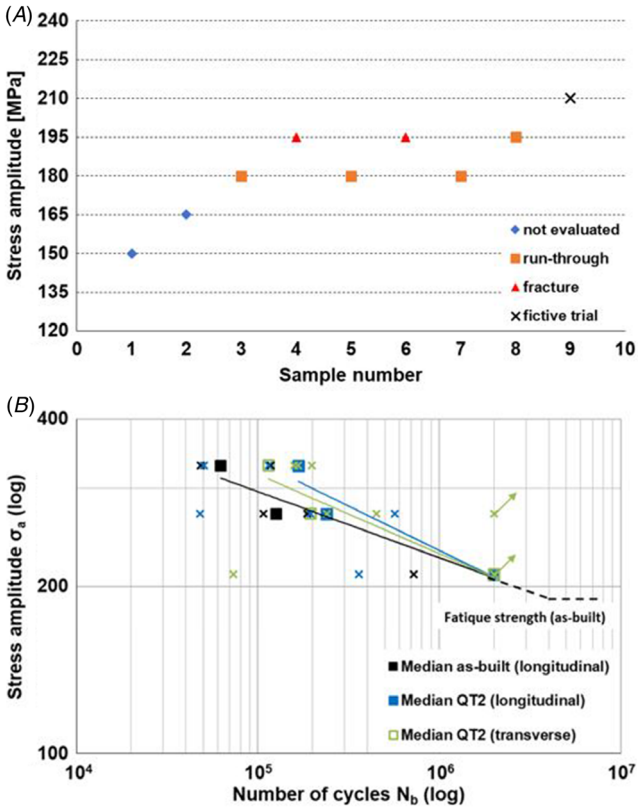

(perpendicular to BD). The trend lines presented in **figure 9*B*** are based on median calculations in order to minimize the influence of outliers.[27] In addition, the experimentally determined values for all stress amplitudes as a function of the material condition are highlighted by crosses. As a result of the quenching and tempering treatment, only a slight improvement of the fatigue performance can be observed in comparison to the as-built condition (**fig. 9*B***). Moreover, an increased scattering occurs in the heat-treated conditons, which can likely be linked to the decrease in ductility and, thus, to a higher notch sensitivity. Interestingly, the trend lines of the longitudinal and transverse directions of the QT2 state are very similar.

Summary

In the present study, a process window for E-PBF processing of quenching and tempering AISI 4140 steel was discussed. The most appropriate process parameters employed led to a high relative density of around 99.94%.

Mechanical tests were conducted using miniature samples. Results obtained revealed that the relatively ductile as-built condition is characterized by a promising mechanical performance with respect to quasistatic as well as cyclic loading. As a result of the microstructural changes induced by the established heat-treatment procedures, a significant increase in fatigue scatter could be observed for the material conditions due to a higher degree of brittleness and, thus, increased notch sensitivity. In fact, results presented clearly highlight significant differences in terms of evolution of quasistatic and fatigue properties. For this reason, characterization of additively manufactured materials has to include all loading scenarios relevant for envisaged applications. Here, the use of miniature samples for assessment seems to be highly promising with respect to the efficiency of testing considering the requirements set by additive manufacturing.

ACKNOWLEDGMENTS

Funding by Deutsche Forschungsgemeinschaft, Grant No. 413259151, is gratefully acknowledged.

References

1. M. Galati and L. Iuliano, "A Literature Review of Powder-Based Electron Beam Melting Focusing on Numerical Simulations," *Additive Manufacturing* 19 (2018): 1–20, https://doi.org/10.1016/j.addma.2017.11.001
2. J. Zhang, *Additive Manufacturing: Materials, Processes, Quantifications and Applications* (San Diego, CA: Elsevier Science, 2018).
3. L. Portolés, O. Jordá, L. Jordá, A. Uriondo, M. Esperon-Miguez, and S. Perinpanayagam, "A Qualification Procedure to Manufacture and Repair Aerospace Parts with Electron Beam Melting," *Journal of Manufacturing Systems* 41 (2016): 65–75, https://doi.org/10.1016/j.jmsy.2016.07.002

4. A. Ataee, Y. Li, D. Fraser, G. Song, and C. Wen, "Anisotropic Ti-6Al-4V Gyroid Scaffolds Manufactured by Electron Beam Melting (EBM) for Bone Implant Applications," *Materials and Design* 137 (2018): 345–354, https://doi.org/10.1016/j.matdes.2017.10.040
5. A. Zadi-Maad, R. Rohib, and A. Irawan, "Additive Manufacturing for Steels: A Review," *Materials Science and Engineering* 285 (2018), https://doi.org/10.1088/1757-899X/285/1/012028
6. S. Biamino, A. Penna, U. Ackelid, S. Sabbadini, O. Tassa, P. Fino, M. Pavese, P. Gennaro, and C. Badini, "Electron Beam Melting of Ti–48Al–2Cr–2Nb SIloy: Microstructure and Mechanical Properties Investigation," *Intermetallics* 19, no. 6 (2011): 776–781, https://doi.org/10.1016/j.intermet.2010.11.017
7. T. McLouth, Y.-W. Chang, J. Wooten, and J.-M. Yang, "The Effects of Electron Beam Melting on the Microstructure and Mechanical Properties of Ti-6Al-4V and Gamma-TiAl," *Microscopy and Microanalysis* 21, no. S3 (2015): 1177–1178, https://doi.org/10.1017/S1431927615006674
8. L. E. Murr, "Metallurgy of Additive Manufacturing: Examples from Electron Beam Melting," *Additive Manufacturing* 5 (2015): 40–53, https://doi.org/10.1016/j.addma.2014.12.002
9. S. Afkhami, M. Dabiri, S. H. Alavi, T. Björk, and A. Salminen, "Fatigue Characteristics of Steels Manufactured by Selective Laser Melting," *International Journal of Fatigue* 122 (2019): 72–83, https://doi.org/10.1016/j.ijfatigue.2018.12.029
10. R. Mines, *Metallic Microlattice Structures* (Cham, Switzerland: Springer International, 2019).
11. P. K. Gokuldoss, S. Kolla, J. Eckert, "Additive Manufacturing Processes: Selective Laser Melting, Electron Beam Melting and Binder Jetting—Selection Guidelines," *Materials (Basel)* 10, no. 6 (2017), https://doi.org/10.3390/ma10060672
12. S. O. Oluwasegun, S. M. Adedayo, L. A. Tunji, M. O. Onuorah, "A Review of Weldability of Carbon Steel in Arc-Based Welding Processes," *Cogent Engineering* 6 (2019), https://doi.org/10.1080/23311916.2019.1609180
13. D. T. Llewellyn and R. C. Hudd, *Steels: Metallurgy and Applications*, 3rd ed. (Boston: Butterworth Heinemann, 1998).
14. G. E. Totten, *Steel Heat Treatment*, 2nd ed. (Boca Raton, FL: CRC Press, 2007).
15. T. DebRoy, H. L. Wei, J. S. Zuback, T. Mukherjee, J. W. Elmer, J. O. Milewski, A. M. Beese, A. Wilson-Heid, A. De, and W. Zhang, "Additive Manufacturing of Metallic Components—Process, Structure and Properties," *Progress in Materials Science* 92 (2018): 112–224, https://doi.org/10.1016/j.pmatsci.2017.10.001
16. M. Hück, "Ein Verbessertes Verfahren für die Auswertung von Treppenstufenversuchen [An Improved Method for Evaluating Stair Step Tests]," *Materials Science and Engineering Technology* 14, no. 12 (1983): 406–417, https://doi.org/10.1002/mawe.19830141207
17. P. Bajaj, A. Hariharan, A. Kini, P. Kürnsteiner, D. Raabe, and E. A. Jägle, "Steels in Additive Manufacturing: A Review of Their Microstructure and Properties," *Materials Science and Engineering A* 772 (2020), https://doi.org/10.1016/j.msea.2019.138633
18. D. Herring and R. Hill, ed., *Heat Treating: Proceedings of the 23rd Heat Treating Society Conference* (Materials Park, OH: ASM International, 2006).
19. V. Savaria, H. Monajati, F. Bridier, and P. Bocher, "Measurement and Correction of Residual Stress Gradients in Aeronautical Gears after Various Induction Surface Hardening Treatments," *Journal of Materials Processing Technology* 220 (2015): 113–123, https://doi.org/10.1016/j.jmatprotec.2014.12.009
20. T. Scharowsky, A. Bauereiß, and C. Körner, "Influence of the Hatching Strategy on Consolidation during Selective Electron Beam Melting of Ti-6Al-4V," *International Journal of Advanced Manufacturing Technology* 92, nos. 5–8 (2017): 2809–2818, https://doi.org/10.1007/s00170-017-0375-1

21. J. Wang, W. J. Wu, W. Jing, X. Tan, G. J. Bi, S. B. Tor, K. F. Leong, C. K. Chua, and E. Liu, "Improvement of Densification and Microstructure of ASTM A131 EH36 Steel Samples Additively Manufactured via Selective Laser Melting with Varying Laser Scanning Speed and Hatch Spacing," *Materials Science and Engineering: A* 746 (2019): 300–313, https://doi.org/10.1016/j.msea.2019.01.019
22. J. Buckstegge, K.-H. Bleses, and H. Preisendanz, "Über die Röntgenographische Bestimmung des Restaustenitgehaltes von Stählen mittels der Untersuchung Mehrphasiger Pulvergemische [About the X-Ray Determination of the Retained Austenite Content of Steeps by Examining Multiphase Powder Mixtures]," *Thyssen Edelstahl Technische Berichte* 6, no. 2 (1980): 143–154.
23. S. Hashmi, *Comprehensive Materials Processing* (Burlington, MA: Elsevier Science, 2014).
24. T. Boukharouba, M. Elboujdaini, and G. Pluvinage, *Damage and Fracture Mechanics: Failure Analysis of Engineering Materials and Structures* (Dordrecht: Springer Netherlands, 2009).
25. D. Greitemeier, F. Palm, F. Syassen, and T. Melz, "Fatigue Performance of Additive Manufactured TiAl6V4 using Electron and Laser Beam Melting," *International Journal of Fatigue* 94 (2017): 211–217, https://doi.org/10.1016/j.ijfatigue.2016.05.001
26. E. Charkaluk and V. Chastand, "Fatigue of Additive Manufacturing Specimens: A Comparison with Casting Processes," *Proceedings* 2, no. 8 (2018): 474–479, https://doi.org/10.3390/ICEM18-05352
27. J. Rosenthal, *Statistics and Data Interpretation for Social Work* (New York: Springer, 2011).